Acta Cryst B
STRUCTURAL SCIENCE
CRYSTAL ENGINEERING
MATERIALS

ISSN 2052-5206

The magnetic structure and spin-reorientation of ErGa

J. M. Cadogan,[a]* D. H. Ryan,[b] R. A. Susilo,[a,c]‡ S. Muñoz Pérez,[a]§ R. Cobas,[a]§ N. R. Lee-Hone,[b] B. R. Hansen[d] and M. Avdeev[e]

[a]School of Science, UNSW Canberra at the Australian Defence Force Academy, Canberra, ACT, BC 2610, Australia, [b]Department of Physics, McGill University, Montreal, QC, H3A 2T8, Canada, [c]Department of Physics, Pohang University of Science and Technology, Pohang, Korea, [d]Institute of Physics, Technical University of Denmark, 2800 Kongens Lyngby, Denmark, and [e]Australian Centre for Neutron Scattering, Australian Nuclear Science and Technology Organisation, PMB 1, Menai NSW 2234, Australia. *Correspondence e-mail: s.cadogan@unsw.edu.au

Received 14 May 2024
Accepted 31 August 2024

Edited by B. J. Campbell, Brigham Young University, USA

This article is part of a focused issue on Magnetic Structures.

‡ Current address: Research Center for Quantum Physics, National Research and Innovation Agency (BRIN), South Tangerang, 15314, Indonesia.
§ Current address: Department of Materials Science and Engineering, University of Toronto, Toronto ON, M5S 3E4, Canada.

Keywords: rare-earth intermetallics; magnetic structures; neutron diffraction; Mössbauer spectroscopy.

Supporting information: this article has supporting information at journals.iucr.org/b

The magnetic structure of the intermetallic compound ErGa has been determined using high-resolution neutron powder diffraction. This compound crystallizes in the orthorhombic (*Cmcm*, No. 63) CrB-type structure and orders ferromagnetically at 32 (2) K, with the Er moments initially aligned along the *b* axis. Upon cooling below 16 K, the Er magnetic moments cant away from the *b* axis towards the *c* axis. At 3 K, the Er moment is 8.7 (3) μ_B and the Er magnetic moments point in the direction 31 (3)° away from the crystallographic *b* axis, within the *bc* plane. ^{166}Er Mössbauer spectroscopy work supports this structure and shows clear signals of the spin-reorientation in both the magnetic and electric quadrupole hyperfine interactions.

1. Introduction

The *R*Ga (*R* = rare earth) intermetallic compounds are known to form as stoichiometric 1:1 line compounds with no evidence for any significant off-stoichiometry (Yatsenko *et al.*, 1979; Massalski *et al.*, 1990). *R*Ga compounds form as the orthorhombic CrB-type *Cmcm* (No. 63) structure with the *R* and Ga atoms both fully occupying 4*c* sites, generated by (0 *y* $\frac{1}{4}$). The *R*Ga series of compounds was first prepared in the 1960s (Iandelli, 1960; Baenziger & Moriarty, 1961; Schob & Parthé, 1965; Dwight *et al.*, 1967) and they order ferromagnetically with Curie temperatures that range from a high of 183 K in GdGa (Shohata, 1977) to a low of 15 K for TmGa (Gao *et al.*, 2013).

The magnetic structures of some of the *R*Ga compounds have been studied using neutron diffraction: TbGa (Cable *et al.*, 1964), ErGa (Barbara *et al.*, 1971), HoGa (Susilo *et al.*, 2012), GdGa (Susilo *et al.*, 2014) and TmGa (Cadogan *et al.*, 2014; Cadogan & Avdeev, 2015).

Mössbauer spectroscopy has also been used to study the magnetic structures of *R*Ga compounds using both rare-earth isotopes ^{155}GdGa (Susilo *et al.*, 2014), ^{161}DyGa (Iraldi *et al.*, 2008) and ^{169}TmGa (Cadogan *et al.*, 2014) and ^{119}Sn. Nesterov *et al.* (1992) used ^{119}Sn Mössbauer spectroscopy on Sn-doped samples to show that NdGa, HoGa and ErGa undergo spin-reorientations upon cooling. This ^{119}Sn Mössbauer work was extended by Delyagin *et al.* (2007). The *R*Ga compounds have attracted some interest due to both their magnetocaloric behaviour (Zhang *et al.*, 2009; Chen *et al.*, 2009, 2010; Zheng *et al.*, 2009; Gao *et al.*, 2013; Mo *et al.*, 2013) and, recently, their modified magnetic behaviour upon hydrogenation (Shtender *et al.*, 2024; Cedervall *et al.*, 2024).

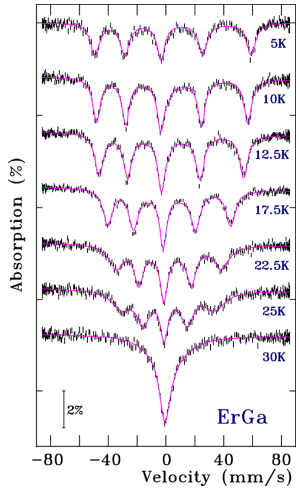

The subject of this paper is ErGa which is a ferromagnet with a Curie temperature of 32 (2) K, the average of values reported by Fujii *et al.* (1971), Barbara *et al.* (1971), Shohata (1977), Nesterov *et al.* (1992), Delyagin *et al.*, (2007) and Chen *et al.* (2009). Single-crystal magnetization measurements on ErGa at 4.2 K by Shohata (1977) indicated that the *b* axis is the easy magnetic axis, which is consistent with the ^{119}Sn Mössbauer spectroscopy results of Nesterov *et al.* (1992) and Delyagin *et al.* (2007). A substantial magnetization along the *c* axis was also observed at 4.2 K by Shohata (1977) and, from the data presented by Shohata, we estimate zero-field Er magnetization components of 175 emu g^{-1} (J/T-kg) along the *b* axis and 100 emu g^{-1} along the *c* axis, yielding a net Er moment of 8.55 μ_B, almost the 'free-ion' value of 9 μ_B. These data also yield a canting angle of 30° from the *b* axis, within the *bc* plane. The magnetization data show a field-induced spin-flip towards the *a* axis at a field of 5 kOe.

The magnetometry results reported by Shohata (1977) are at odds with an earlier neutron diffraction study of ErGa carried out at 4.2 K by Barbara *et al.* (1971) who reported an *ab* planar canted magnetic structure with ferromagnetism along the *a* axis and antiferromagnetism along the *b* axis, with a canting angle of 34 (3)° from the *a* axis (Barbara *et al.*, 1971).

In this paper we aim to resolve this discrepancy by re-examining the magnetic structure and spin reorientation in ErGa using a combination of high-resolution neutron powder diffraction and ^{166}Er Mössbauer spectroscopy. We shall also show that our magnetic structure is fully consistent with the aforementioned ^{119}Sn Mössbauer work.

2. Experimental

The ErGa sample was prepared in an argon-arc furnace. Stoichiometric amounts of the pure elements Er (99.9%) and Ga (99.999%) were melted several times under pure (less than 1 p.p.m. impurity) argon to ensure homogeneity. X-ray powder diffraction was carried out at room temperature on a PANalytical X'Pert Pro diffractometer using Cu *Kα* radiation. Neutron powder diffraction patterns were obtained on the Echidna high-resolution powder diffractometer at the OPAL reactor in Sydney, Australia (Liss *et al.*, 2006; Avdeev & Hester, 2018). The neutron wavelength was 2.4395 (5) Å. The neutron diffraction data were corrected for absorption effects and all patterns were refined using the Rietveld method and *FullProf/WinPlotr* (Rodríguez-Carvajal, 1993; Roisnel & Rodríguez-Carvajal, 2001).

^{166}Er Mössbauer spectra were acquired using 1 GBq ^{166}Ho sources prepared by neutron activation of $Ho_{0.6}Y_{0.4}H_2$ in the SLOWPOKE reactor at the Ecole Polytechnique, Montréal, Canada. The spectrometer was operated vertically with both the source and sample cooled in a helium-flow cryostat. Independent temperature control of the source was used to keep it at or above 5 K to avoid relaxation-induced line broadening which we have observed at lower source temperatures. Velocity calibration of all Mössbauer spectra was carried out using an He/Ne laser interferometer. With the drive system of the spectrometer operating in sinusoidal-mode, the calibration drift at a maximum Doppler velocity of 82 mm s^{-1} was less than 0.02 s^{-1}. Velocity calibration was cross-checked against both $ErFe_2$ at our operating velocity and ^{57}Co**Rh**/*α*-Fe at lower velocities. [For the benefit of those readers unfamiliar with ^{166}Er Mössbauer spectroscopy, the spectra are acquired using the 80.56 keV, $2^+ \rightarrow 0^+$, γ transition, giving rise to a five-line spectrum in the presence of a magnetic hyperfine field (Cadogan & Ryan, 2004).] Velocity calibration was cross-checked using the 819.4 T magnetic hyperfine splitting at 4 K in the cubic Laves compound $ErFe_2$ [based on ^{166}Er Mössbauer and ^{167}Er NMR measurements by Hodges *et al.* (1981) and Berthier & Devine (1981), respectively]. All ^{166}Er spectra were fitted using a nonlinear least-squares minimization routine with line positions and intensities derived from a full solution to the nuclear hyperfine Hamiltonian for the ^{166}Er $2^+ \rightarrow 0^+$ transition (Voyer & Ryan, 2006).

3. Results

Refinement of the X-ray powder diffraction pattern obtained at 295 K confirmed the formation of the CrB-type *Cmcm* (No. 63) orthorhombic phase. Traces of the impurity phases Er_2O_3 (cubic, $Ia\bar{3}$, $a \approx 10.5$ Å), Er_3Ga_5 (orthorhombic *Pnma*, $a \approx 11.3$ Å, $b \approx 9.6$ Å, $c \approx 6.0$ Å) and Er_5Ga_3 (hexagonal, $P6_3/mcm$, $a \approx 8.5$ Å, $c \approx 6.4$ Å) were observed and a co-refinement of the X-ray and neutron powder diffraction patterns indicated a total impurity content of about 3 wt%. The refined unit-cell parameters of ErGa at 295 K are a = 4.2619 (2) Å, b = 10.7349 (3) Å and c = 4.0320 (2) Å.

3.1. Neutron diffraction

In Fig. 1, we show the refined neutron powder diffraction pattern of ErGa obtained at 40 K, above the Curie temperature of 32 K (Shohata, 1977) and the atomic position parameters for ErGa derived from the refinement of the 40 K

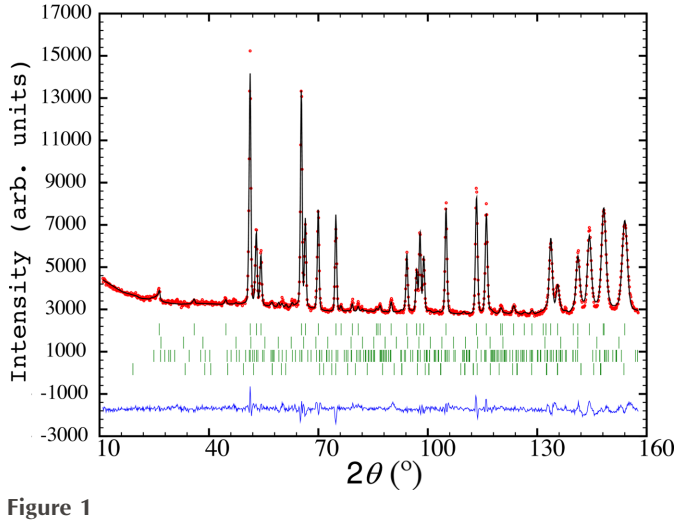

Figure 1
Refined neutron powder diffraction pattern of ErGa obtained at 40 K with a neutron wavelength of 2.4395 (5) Å. The lowest three sets of Bragg markers represent the contributions from the minor impurities Er_2O_3, Er_3Ga_5 and Er_5Ga_3.

Table 1
Crystallographic data (at 40 K) for ErGa in the orthorhombic *Cmcm* cell, refined from the neutron diffraction pattern.

Atom	Site	Point symmetry	x	y	z
Er	4*c*	*m*2*m*	0	0.3586 (4)	0.25
Ga	4*c*	*m*2*m*	0	0.0763 (4)	0.25
a, *b*, *c* (Å)		4.2535 (2),	10.6968 (5),	4.0157 (3)	

Table 2
Crystallographic data (at 3 K) for ErGa in the orthorhombic *Cmcm* cell, refined from the neutron diffraction pattern.

Atom	Site	Point symmetry	x	y	z
Er	4*c*	*m*2*m*	0	0.3583 (4)	0.25
Ga	4*c*	*m*2*m*	0	0.0752 (4)	0.25
a, *b*, *c* (Å)		4.2527 (2),	10.6913 (5),	4.0157 (3)	

neutron diffraction pattern are given in Table 1. The conventional R factors for this refinement are $R_F = 4.62\%$ and $R_{\rm Bragg} = 5.32\%$. The isotropic atomic displacement parameters are 0.23 (10) Å^2 and 0.74 (12) Å^2 for Er and Ga, respectively. An alternative fitting using a single, overall atomic displacement parameter gave 0.47 (11) Å^2 and virtually identical fits.

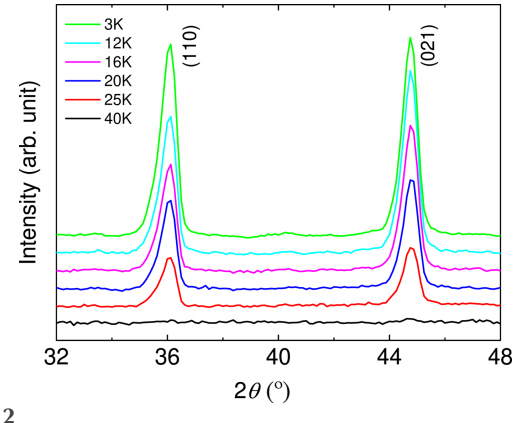

Figure 2
Section of the neutron powder diffraction patterns of ErGa obtained at 40 K, 25 K, 20 K, 16 K, 12 K and 3 K, with a neutron wavelength of 2.4395 (5) Å, showing the two prominent magnetic reflections 110 and 021. The patterns have been offset vertically for clarity.

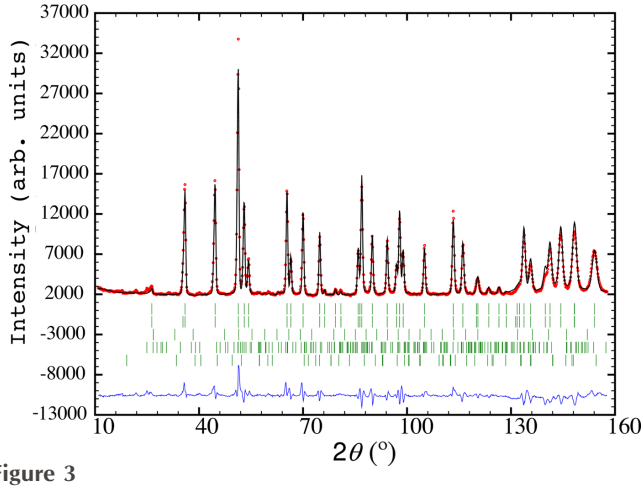

Figure 3
Refined neutron powder diffraction pattern of ErGa obtained at 3 K, with a neutron wavelength of 2.4395 (5) Å. The red dots are the experimental diffraction data, the black line is the Rietveld fit and the blue line shows the difference between the experiment and the fit. The green bars are Bragg markers showing the contributions from (top to bottom) ErGa (nuclear), ErGa (magnetic), and the minor impurities Er_2O_3, Er_3Ga_5 and Er_5Ga_3.

In Fig. 2, a section of the neutron powder diffraction patterns of ErGa, obtained at 40 K, 25 K, 20 K, 16 K, 12 K and 3 K is shown. The patterns obtained at 25 K and below show considerable magnetic contributions, particularly to the 110 and 021 reflections (Fig. 2).

The refined neutron powder diffraction pattern of ErGa obtained at 3 K is shown in Fig. 3 and the atomic position parameters for ErGa derived from the refinement of the 3 K neutron diffraction pattern are given in Table 2. Due to the presence of magnetic scattering in patterns obtained below the Curie temperature, the isotropic atomic displacement parameters were not refined. Rather, we adopted the approach recommended in the *FullProf* manual of fixing an overall atomic parameter to a physically reasonable value, in this case 0.08 Å^2 at 3 K, based on scaling our paramagnetic 40 K results. In the Rietveld refinement of the diffraction data in the non-magnetic regime, we saw no evidence for partial site occupancies, so all refinements of the magnetic diffraction data used the well established 1:1 stoichiometry.

As mentioned above, the diffraction patterns obtained at 25 K and below show considerable magnetic contributions from the Er sublattice. There are no additional reflections that might signal antiferromagnetic order and all magnetic contributions add to the existing Bragg nuclear reflections, *i.e.* the propagation vector **k** is [0 0 0]. The dominant magnetic contributions occur at the 110 and 021 reflections, with scattering angles $2\theta = 36.0^\circ$ and 44.6°, respectively, as shown in Fig. 2.

In order to consider all possible magnetic structures allowed for ErGa, we carried out representational analysis for the Er site using the *BASIREPS* program, which is part of the *FullProf/WinPlotr* suite (Rodríguez-Carvajal, 1993; Roisnel & Rodríguez-Carvajal, 2001). The decomposition of the magnetic representation, above the spin-reorientation temperature, comprises six one-dimensional irreducible representations (irreps):

$$\Gamma_{\rm mag}^{4c} = 1\Gamma_2^{(1)} + 1\Gamma_3^{(1)} + 1\Gamma_4^{(1)} + 1\Gamma_5^{(1)} + 1\Gamma_7^{(1)} + 1\Gamma_8^{(1)} \qquad (1)$$

and the basis vectors of these irreps are given in Table 3.

The antiferromagnetic modes Γ_2, Γ_4 and Γ_8 can be ruled out on the strength of the magnetometry and neutron diffraction work that clearly indicates ferromagnetic order. Therefore, we are left with ferromagnetic order along one of the orthorhombic crystal axes, above the spin-reorientation temperature. The absence of magnetic contributions to the 020 and 040 reflections indicates ferromagnetic order along the *b* axis. At

Table 3
Representational analysis for the Er (4*c*) site in ErGa with a propagation vector [0 0 0].

The respective Er atomic positions are (0, y, $\frac{1}{4}$), (0, $-y$, $\frac{3}{4}$), ($\frac{1}{2}$, $\frac{1}{2}+y$, $\frac{1}{4}$) and ($\frac{1}{2}$, $\frac{1}{2}-y$, $\frac{3}{4}$).

Representation	Ordering mode	Magnetic space group (MSG)	Bilbao IR	Moment arrangement
Γ_2	G_b	$Cm'c'm'$	mGM1−	+ − + −
Γ_3	F_c	$Cm'c'm$	mGM2+	+ + + +
Γ_4	G_a	$Cm\,c\,m'$	mGM2−	+ − + −
Γ_5	F_b	$Cm'c\,m'$	mGM4+	+ + + +
Γ_7	F_a	$Cm\,c'm'$	mGM3+	+ + + +
Γ_8	G_c	$Cm'cm$	mGM3−	+ − + −

20 K (just above the spin-reorientation temperature), a refined Er magnetic moment of 5.4 (2) μ_B is obtained. The conventional R factors for the 20 K refinement are R_F = 4.65%, R_{Bragg} = 6.29% and R_{mag} = 8.96%. The magnetic space group (MSG) describing this *b*-axis ferromagnetic order is $Cm'cm'$ (Γ_5), involving the mGM4+ irrep in the Bilbao notation, MSG = No. 63.464 in BNS notation (Belov *et al.*, 1957) or No. 63.8.518 in OG notation (Opechowski & Guccione, 1965; Litvin, 1998). See also Campbell *et al.* (2022).

Upon cooling below 20 K we observed a marked change in the intensities of the 110 and 021 reflections, together with the appearance of magnetic contributions to the 020 and 040 reflections (see Fig. 4), indicating that the magnetic order of the Er sublattice is no longer aligned along the *b* axis. This spin-reorientation has also been observed in ac susceptibility measurements (Chen *et al.*, 2009). No evidence of peak splitting or undue broadening was seen, even up to 2θ = 155° where the Er magnetic form factor is negligible, that would suggest any magnetoelastic distortion that might reduce the lattice symmetry from orthorhombic.

Our refinement of the neutron diffraction pattern obtained at 3 K shows that the Er magnetic moments are canted away from the *b* axis by 31 (3)°, within the *bc* plane. The conventional R factors for this refinement are R_F = 6.1%, R_{Bragg} = 10.4%, R_{mag} = 10.0%. The Er moment is 8.7 (3) μ_B at 3 K, *i.e.* the 'free-ion' value ($g_J J \rightarrow 9\ \mu_B$). Below the spin-reorientation, the magnetic order may be thought of as a mixing of the $Cm'cm'$ *b*-axis order [mGM4+ Bilbao irrep] and the $Cm'c'm$ (MSG = No. 63.462 BNS; No. 63.6.516 OG) *c*-axis order (mGM2+ Bilbao IR), yielding the canted magnetic space group $C2'/m'$ (MSG = No. 12.62 BNS; No. 12.5.70 OG), obtained using the routine *k-SUBGROUPSMAG*, a module of the Bilbao Crystallographic Server (Perez-Mato *et al.*, 2015).

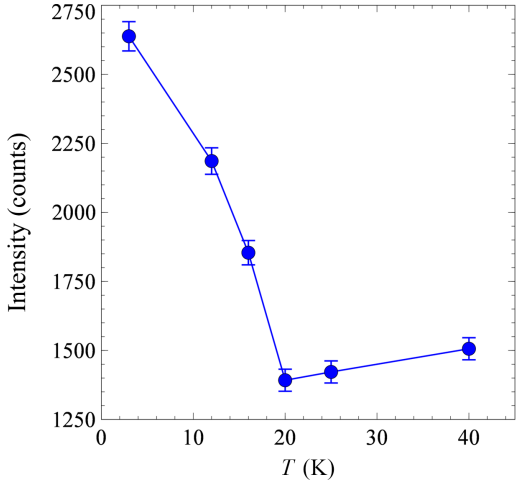

Figure 4
Temperature dependence of the integrated intensity of the 040 reflection at $2\theta \approx 54.3°$ in the neutron powder diffraction patterns of ErGa. The solid line is merely a visual guide.

Table 4
Magnetic data for ErGa (θ and ϕ are the conventional polar angles (°) relative to the *abc* crystal frame).

T (K)	Er moment (μ_B)	θ (°)	ϕ (°)
40	0	–	–
25	3.9 (2)	90	90
20	5.4 (2)	90	90
16	6.4 (2)	66 (3)	90 (4)
12	7.2 (2)	62 (3)	90 (4)
3	8.7 (3)	59 (3)	90 (4)

For comparison, the second-best refinement gave R_{mag} = 15.2% for a [0 F_b G_c] ordering mode. A refinement using the structure reported by Barbara *et al.* (1971), detailed in the *Introduction*, gave R_{mag} = 39%.

In Table 4, the magnetic moments and orientations of the Er moments in ErGa are presented, deduced from the refinements of the neutron diffraction patterns. The Er magnetic moment at 3 K, relative to the crystallographic axes, is [0, 7.5 (5), 4.5 (5)] μ_B.

Finally, we observe signs of magnetic ordering in the Er_3Ga_5 and Er_5Ga_3 impurities, although their contributions are far too weak for a proper analysis. Below 25 K, a small peak appears at a *d*-spacing of around 6.35 Å which could correspond to a 001 reflection from the Er_5Ga_3 $P6_3/mcm$ cell, a reflection that is not allowed for this space group, suggesting antiferromagnetism, which is consistent with a report of antiferromagnetic order at 23 K in Er_5Ga_3 by Konguetsof & Yakinthos (1982). A second, weak, impurity magnetic peak is present at 20 K and below, with a *d*-spacing of around 5.6 Å, that might correspond to a (200) reflection from the Er_3Ga_5 *Pnma* cell.

3.2. ^{166}Er Mössbauer spectroscopy

In Fig. 5, we show our ^{166}Er Mössbauer spectra obtained over the temperature range 5–35 K and in Fig. 6 we show the temperature dependences of the ^{166}Er hyperfine magnetic field and the electric quadrupole splitting parameter eQV_{ZZ}. It is immediately apparent in both hyperfine parameters that there is a change in the magnetic order of ErGa at around 16 K (the spin-reorientation), and this is particularly pronounced in the eQV_{ZZ} data. The temperature dependences of the ^{166}Er hyperfine magnetic field and electric quadrupole splitting parameter eQV_{ZZ} are proportional to the thermal ensemble averages $\langle \hat{J}_z \rangle$ and $\langle 3\hat{J}_z^2 - \hat{J}^2 \rangle$ (using standard nota-

tion) over the 4*f* electrons, respectively, and these quantities will be discussed in Section 3.4 where we consider the crystal field acting on the Er.

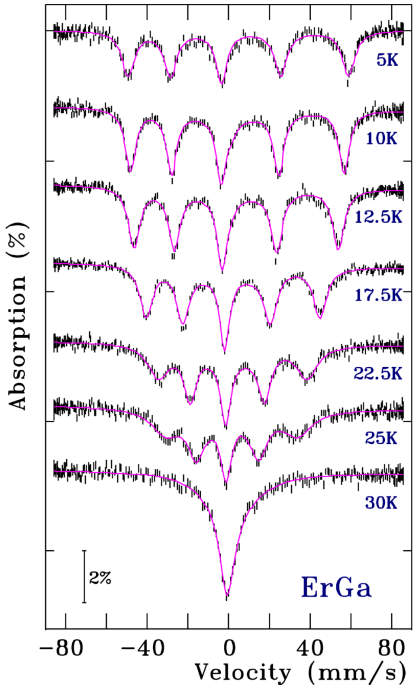

Figure 5
^{166}Er Mössbauer spectra of ErGa as a function of temperature. The solid lines are fits as described in the text.

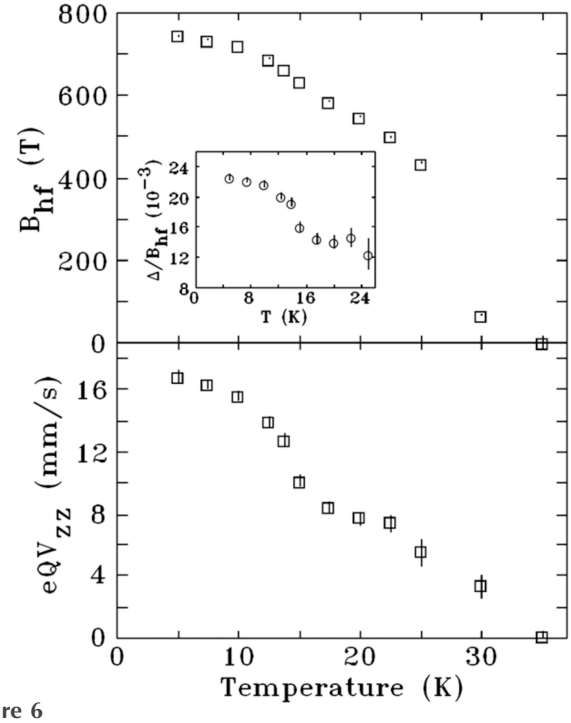

Figure 6
Temperature dependences of the magnetic hyperfine field (top) and the electric field gradient parameter eQV_{ZZ} (bottom) at the ^{166}Er nuclei in ErGa. The inset in the top panel shows the ratio of the quadrupole splitting to the hyperfine field.

The ^{166}Er quadrupole splitting parameter eQV_{ZZ} shows a strong temperature dependence as seen in Fig. 6. As in the case of the temperature dependence of hyperfine field, a break in slope is also clearly visible at ∼16 K, associated with the spin-reorientation transition. The sudden increase in eQV_{ZZ} of about ∼5 mm s^{-1} between 17 K and 10 K signals a change in the Er moment direction and is due to the change in the expectation value of the Stevens operator equivalent $\langle O_{20}\rangle$ caused by the crystal field interaction, as will be discussed below.

In its simplest form, the electric quadrupole interaction acting on the ^{166}Er nucleus has a large contribution from the 4f electrons of the Er ion and a weaker contribution from the surrounding lattice charges. Treating the lattice term as a perturbation on the dominant 4*f* term, we may write (Sanchez *et al.*, 1986):

$$eQV_{ZZ} = eQV_{ZZ}^{4f} + \tfrac{1}{2}eQV_{ZZ}^{\rm lattice}\left[3\cos^2\alpha - 1 + \eta^{\rm lattice}(\sin^2\alpha)\cos(2\beta)\right] \quad (2)$$

Here, (α, β) are the polar angles of the hyperfine magnetic field in the principal axis frame of the EFG at the ^{166}Er nuclei.

We can estimate the lattice contribution to the EFG at the ^{166}Er nuclei from our previous ^{155}Gd Mössbauer study of GdGa in which the measured EFG is purely lattice-driven since Gd^{3+} is an S-state ion.

The measured eQV_{ZZ} at the ^{155}Gd nuclei in GdGa at 4 K is −1.42 (5) mm s^{-1} and the value relevant to ^{166}Er may be estimated by:

$$eQV_{ZZ}^{\rm lattice}({\rm Er}) = eQV_{ZZ}^{\rm lattice}({\rm Gd}) \times \frac{Q({\rm Er})}{Q({\rm Gd})} \times \frac{E_\gamma({\rm Gd})}{E_\gamma({\rm Er})} \quad (3)$$

(The inclusion of the γ-ray energies E_γ in the above expression is a consequence of the use of Mössbauer units of mm s^{-1}). The respective nuclear quadrupole moments (Q) are +1.27 (3)*b* (^{155}Gd $\frac{3}{2}^-$ ground state) and −1.9 (4)*b* (^{166}Er 2^+ first excited state) (data taken from Stone, 2021) and the respective γ-ray energies (E_γ) are 86.55 keV (^{155}Gd) and 80.58 keV (^{166}Er) (Nuclear Data Centre Japan, 2011). Hence, we find $eQV_{ZZ}^{\rm lattice}$(Er) = +2.28 (58) mm s^{-1} and using the angles given in Table 4, we estimate that $eQV_{ZZ}^{\rm lattice}$ accounts for less than 10% of the observed change in eQV_{ZZ}.

3.3. ^{119}Sn Mössbauer spectroscopy

As a further check of our magnetic structures we now consider the ^{119}Sn Mössbauer spectroscopy results obtained by doping the *R*Ga compounds with ^{119}Sn reported by (Nesterov *et al.*, 1992) and (Delyagin *et al.*, 2007). The Sn dopant is non-magnetic and substitutes for the Ga so any hyperfine field at this dopant site is transferred from the magnetic order of the neighbouring *R* sublattice. Information about the magnetic ordering direction of the *R* moments can be deduced by determining the orientation of the hyperfine field (assumed collinear with the *R* magnetic order) within the principal axis frame of the Electric Field Gradient (EFG) at the ^{119}Sn site.

The principal axis of the EFG is defined such that the diagonal components of the EFG tensor *i.e.* V_{XX}, V_{YY} and V_{ZZ}, are related thus:

$$|V_{XX}| \leq |V_{YY}| \leq |V_{ZZ}|$$

and the asymmetry parameter η of the EFG tensor is:

$$\eta = \frac{V_{XX} - V_{YY}}{V_{ZZ}}$$

leading to $0 < \eta < 1$. Delyagin *et al.* (2007) showed that the EFG axes at the Ga (^{119}Sn) 4*c* sites are aligned along the orthorhombic axes, as expected from the *m2m* point symmetry of these sites, although the precise axial assignments cannot be specified *a priori*. The particular identification of the EFG axes can be determined from the measured hyperfine parameters and is (*XYZ*) = (*bca*) at the Ga(^{119}Sn) 4*c* sites (Delyagin *et al.*, 2007). Within this EFG frame, the temperature dependence of the ^{119}Sn quadrupole splitting showed that above about 20 K the hyperfine field makes an angle of 90° with the *Z*(EFG) axis and is oriented along the *X*(EFG) axis. In other words, Er magnetic ordering is along the crystal *b* axis, in agreement with the single-crystal magnetization work of Shohata (1977) and also as we found by neutron diffraction. Below 20 K, this angle decreases gradually, reaching about 60° at 5 K, with the hyperfine field lying in the *XY*(EFG) plane, *i.e.* Er magnetic order in the crystal *bc* plane, again in full agreement with our neutron diffraction results. In Fig. 7, the orientational relationship is shown between the Mössbauer and neutron diffraction measurements, in terms of the crystal (*abc*) and EFG (*XYZ*) axes at the Ga 4*c* sites.

The quadrupole shift (QSH) in a magnetically split Mössbauer spectrum, as defined by Delyagin *et al.* (2007), is

$$\mathrm{QSH} = \frac{eQV_{ZZ}}{8} \times [3\cos^2\alpha - 1 + \eta(\sin^2\alpha)\cos(2\beta)] \quad (3)$$

using standard notation. Here, (α, β) are the polar angles of the hyperfine magnetic field in the principal axis frame of the EFG at the ^{119}Sn nuclei. As shown in our previous work on HoGa (Susilo *et al.*, 2012), there is a simple correspondence between the polar angles (θ, ϕ) that describe the orientation of the hyperfine field (assumed collinear with the R magnetic moment) in the crystal (*abc*) frame and the polar angles (α, β) describing that orientation in the EFG principal frame

$$\alpha = \arccos[\sin\theta\cos\phi] \quad (4)$$

$$\beta = \arctan\left[\frac{\cos\theta}{\sin\theta\sin\phi}\right]. \quad (5)$$

Using the accepted conventions for describing the components of the EFG tensor, Delyagin *et al.* (2007) deduced eQV_{ZZ} = 1.10 (8) mm s^{-1} and η = 0.65 (9) at the Ga (^{119}Sn) site. Thus, above the spin-reorientation we take θ = 90° and ϕ = 90°, corresponding to *b*-axis order, and so α = 90° and β = 0° in the ^{119}Sn EFG frame and hence we deduce QSH = −0.048 mm s^{-1}, which compares very well with the experimentally observed value of −0.040 (6) mm s^{-1}.

Below the spin-reorientation, we can take θ = 60° and ϕ = 90°, corresponding to canting in the *bc* plane, and so α = 90° and β = 31° in the ^{119}Sn EFG frame and we calculate QSH = −0.093 mm s^{-1}, which compares very well with the experimentally observed value of −0.075 (6) mm s^{-1} at 5 K. To reproduce the experimental ^{119}Sn QSH value, we require β = 23 (3)° which corresponds to a canting angle of θ = 67 (3)°, consistent with our neutron diffraction measurement of 59 (3)°.

If we take the ErGa magnetic structure reported by Barbara *et al.* (1971) we find θ = 90° and ϕ = ± 34°, corresponding to canting in the *ab* plane, and so α = 34° and β = 0° in the ^{119}Sn EFG frame, leading to a calculated QSH = +0.174 mm s^{-1}, which has the opposite sign and more than twice the magnitude of the experimentally observed QSH value of −0.075 (6) mm s^{-1}.

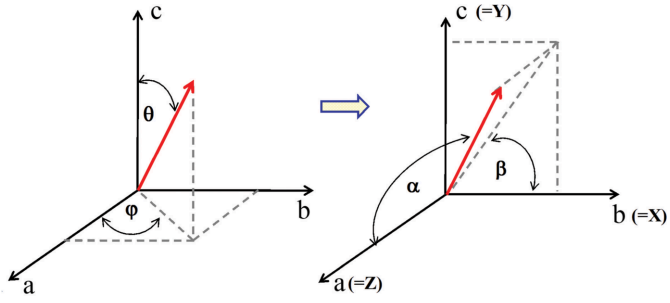

Figure 7
Orientation of the Er magnetic moment (and hence hyperfine field at the ^{119}Sn sites) relative to the crystal (*abc*) and EFG(*XYZ*) axes, used in the interpretation of the neutron powder diffraction and Mössbauer data.

3.4. The crystal field in ErGa

The spin-reorientation observed in ErGa is driven by competition between the different crystal-field orders acting on the Er, with the higher-order (4th and 6th) terms becoming increasingly significant as the temperature is lowered. The observation of *b*-axis order just below T_c is consistent with the sign of the second-order crystal-field terms derived from single-crystal susceptibility measurements by Shohata (1977), as will be shown below.

Using standard notation (Hutchings, 1964), the crystal-field Hamiltonian acting on the Er can be written as:

$$\mathcal{H}_{\mathrm{cf}} = \sum_{n=2,4,6}\sum_{m=0}^{n} B_{nm}O_{nm} = \sum_{n=2,4,6}\sum_{m=0}^{n} \theta_n\langle r^n\rangle A_{nm}O_{nm}, \quad (6)$$

where B_{nm} are the crystal-field parameters and the O_{nm} are the spin operators (Stevens notation). The A_{nm} are lattice summations and θ_n are the Stevens coefficients (n = 2, 4, 6) of the Er^{3+} ion. The $\langle r^n\rangle$ are the 4*f*-electron radial averages (Freeman & Desclaux, 1979). For the point symmetry *m*2*m* of the Er 4*c* site, the crystal-field Hamiltonian becomes:

$$\begin{aligned}\mathcal{H}_{\mathrm{cf}} = {} & B_{20}O_{20} + B_{22}O_{22} + B_{40}O_{40} + B_{42}O_{42} + B_{44}O_{44} \\ & + B_{60}O_{60} + B_{62}O_{62} + B_{64}O_{64} + B_{66}O_{66}. \end{aligned} \quad (7)$$

At this point, further progress is hampered by the need for nine crystal field parameters, in addition to the molecular field acting on the Er. As a first approximation, we can estimate the molecular field from the measured Curie temperature of 32 K by assuming a simple $J = 15/2$ Brillouin function and ignoring crystal-field effects. Thus, we estimate the molecular field on the Er ion to be about 14 T at $T = 0$ K. Estimating the crystal-field parameters is, however, not as straightforward.

Shohata (1977) measured the *ac*-susceptibility of a single-crystal of ErGa along the three crystallographic axes (*abc*) and one can use this information to estimate the second-order crystal field terms acting on the Er ion. As outlined in the papers by Boutron (1969) and Bowden *et al.* (1971) the paramagnetic Curie temperatures along the *a*, *b* and *c* axes of a single-crystal can be written as:

$$\theta_a = \theta + (2J-1)(2J+3)(B_{20} + B_{22})/10\,k_B$$

$$\theta_b = \theta - (2J-1)(2J+3)B_{20}/\,5k_B$$

$$\theta_c = \theta + (2J-1)(2J+3)(B_{20} - B_{22})/10\,k_B$$

where θ is the paramagnetic Curie temperature in the absence of crystal-field effects, J is the total angular momentum of the Er ion ($J = 15/2$) and k_B is Boltzmann's constant. It is implicit in the above equation that the principal Z-axis of the crystal-field is taken to be the crystallographic *b* axis. The measured values of the paramagnetic Curie temperatures are $\theta_a = \theta_b =$ 35 K and $\theta_c = 12$ K which yield crystal-field parameters of $B_{20} = -0.15$ K and $B_{22} = -3B_{20} = +0.45$ K. The choice of Z parallel to *b* is clearly not the accepted principal axis frame of the EFG, using standard convention as outlined earlier, since the magnitude of the off-diagonal crystal-field term is greater than that of the diagonal term, *i.e.* $|B_{22}| > |B_{20}|$. The ratio $|B_{22}/B_{20}|$ is effectively just the EFG asymmetry parameter η defined earlier so the choice of axes used in the analysis of the single-crystal *ac*-susceptibility data leads to $\eta > 1$. If we rotate the crystal-field frame so that the new Z axis is the crystallographic *c* axis we obtain $B_{20} = +0.30$ K and $B_{22} = 0$, *i.e.* the principal EFG frame. Furthermore, these parameters yield an EFG asymmetry parameter η of zero in the rotated frame. We note here that the observation of $\eta(\mathrm{Er}) = 0$ is not a consequence of the orthorhombic *m*2*m* point symmetry of the Er site.

We are now left with the task of estimating the various 4th and 6th order crystal field parameters and, in the absence of experimental data, we can begin with simple point-charge calculations, purely as a 'proof-of-principle' exercise. However, it should be emphasized here that ErGa is a metallic compound so a simple point-charge model cannot be considered rigorous. We fixed the ratios of the off-diagonal terms to the diagonal term within a particular order, *e.g.* B_{42}/B_{40} to the values given by a simple point-charge summation over all ions within a sphere of radius 15 Å around the Er site. Of course, we do not know the values of the effective point charges on the Er and Ga, given the metallic nature of ErGa and concomitant effects such as the role played by the conduction electrons. Hence, we simply chose effective point charges of 1.6|*e*| and 0.9|*e*| for Er and Ga, respectively, purely to reproduce the experimental values of B_{20} and B_{22} deduced from the single-crystal susceptibility data of Shohata (1977).

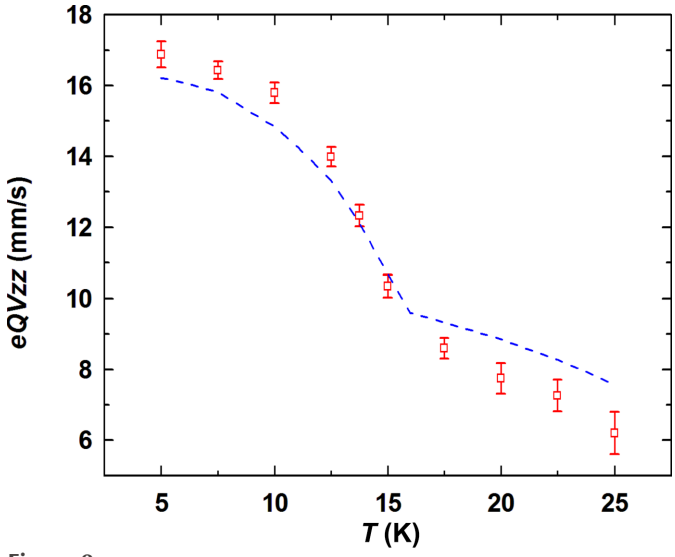

Figure 8
Temperature dependence of the experimental ^{166}Er electric quadrupole parameter eQV_{ZZ} (red symbols) compared to the point-charge crystal field calculation of $<O_{20}>$ ($= \langle 3\hat{J}_z^2 - \hat{J}^2\rangle$) (blue dashed line) for ErGa.

In Fig. 8 we show the temperature dependence of the experimental ^{166}Er electric quadrupole parameter eQV_{ZZ}, calculated from the expectation value $\langle O_{20}\rangle_{4f}$ obtained from point charge summations with $B_{40} = -2$ mK and $B_{60} = -4$ µK. The sudden increase in $eQVzz$ is clearly visible around 15 K. We therefore suggest that the increase in the experimental value of $eQVzz$ for ^{166}Er at the spin-reorientation is predominantly due to the change in the expectation value of $\langle O_{20}\rangle_{4f}$, caused by the crystal field interaction, with the lattice contribution playing a minor role. Once again, we caution that this rather simple, point-charge, crystal field treatment is by no means rigorous and is merely a 'proof-of-principle' exercise at this stage.

4. Conclusions

We have used high-resolution neutron powder diffraction and ^{166}Er Mössbauer spectroscopy to show that the initial magnetic order of the Er sublattice in ErGa is ferromagnetic along the orthorhombic *b* axis below the Curie temperature of 32 K. Upon cooling below 16 K, the Er moments cant away from the *b* axis towards the *c* axis, within the *bc* plane, and at 3 K the Er magnetic order is defined by the polar angles $\theta =$ 59 (3)° and $\phi = 90$ (4)°, relative to the orthorhombic *abc* axes.

Acknowledgements

This work was supported by the University of New South Wales (JMC, RAS, SMP, RC), the Australian Institute of Nuclear Science and Engineering (JMC), the Australian

Nuclear Science and Technology Organisation (JMC, MA), the Natural Sciences and Engineering Research Council of Canada (DHR), Fonds Québécois de la Recherche sur la Nature et les Technologies (DHR) and the Danish Research Council for Nature and Universe (Danscatt) (BRH). DHR is grateful to Dr G. Kennedy at the Ecole Polytechnique SLOWPOKE reactor facility, Montréal, where the activation of the ^{166}Ho sources used in this study was carried out.

References

Avdeev, M. & Hester, J. R. (2018). *J. Appl. Cryst.* **51**, 1597–1604.
Baenziger, N. C. & Moriarty, J. L. (1961). *Acta Cryst.* **14**, 946–947.
Barbara, B., Bècle, C., Nguyen, N. N. & Siaud, E. (1971). *Conf. Digest No. 3: Rare-Earths and Actinides*, pp. 219–221. Institute of Physics, Durham.
Barbara, B., Nguyen, V. N. & Siaud, E. (1972). *C. R. Acad. Sci.* **B274**, 1053–1056.
Belov, N. V., Neronova, N. N. & Smirnova, T. S. (1957). *Sov. Phys. Crystallogr.* **2**, 311–322.
Berthier, Y. & Devine, R. A. B. (1981). *J. Appl. Phys.* **52**, 2071–2073.
Boutron, P. (1969). *J. Phys. Fr.* **30**, 413–419.
Bowden, G. J., Bunbury, D. St P. & McCausland, M. A. H. (1971). *J. Phys. C. Solid State Phys.* **4**, 1840–1854.
Cable, J. W., Koehler, W. C. & Wollan, E. O. (1964). *Phys. Rev.* **136**, A240–A242.
Cadogan, J. M. & Avdeev, M. (2015). *First-Order Magnetic Phase Transition in TmGa.* In *Proceedings of 39th Annual Condensed Matter and Materials Meeting*, 3–6 February 2015, Wagga Wagga, NSW, Australia https://drive.google.com/drive/folders/1su6xkAUv4kzOGN-MwpdDp6aouLMhtlCv.
Cadogan, J. M. & Ryan, D. H. (2004). *Hyperfine Interact.* **153**, 25–41.
Cadogan, J. M., Stewart, G. A., Muñoz Pérez, S., Cobas, R., Hansen, B. R., Avdeev, M. & Hutchison, W. D. (2014). *J. Phys. Condens. Matter*, **26**, 116002.
Campbell, B. J., Stokes, H. T., Perez-Mato, J. M. & Rodríguez-Carvajal, J. (2022). *Acta Cryst.* A**78**, 99–106.
Cedervall, J., Shtender, V., Manuel, P., Pomjakushin, V., Mathieu, R., Häussermann, U. & Andersson, M. S. (2024). *Phys. Rev. B*, **109**, 134434.
Chen, J., Shen, B. G., Dong, Q. Y., Hu, F. X. & Sun, J. R. (2009). *Appl. Phys. Lett.* **95**, 132504.
Chen, J., Shen, B. G., Dong, Q. Y. & Sun, J. R. (2010). *Solid State Commun.* **150**, 157–159.
Delyagin, N. N., Krylov, V. I. & Rozantsev, I. N. (2007). *J. Magn. Magn. Mater.* **308**, 74–79.
Dwight, A. E., Downey, J. W. & Conner, R. A. (1967). *Acta Cryst.* **23**, 860–862.
Freeman, A. J. & Desclaux, J. P. (1979). *J. Magn. Magn. Mater.* **12**, 11–21.
Fujii, H., Shohata, N., Okamoto, T. & Tatsumoto, E. (1971). *J. Phys. Soc. Jpn*, **31**, 1592.
Gao, T., Nishimura, K., Matsumoto, T., Namiki, T. & Isikawa, Y. (2013). *Solid State Commun.* **158**, 1–4.
Hodges, J. A., Jehanno, G., Schuhl, A. & Berthier, Y. (1981). *Hyperfine Interact.* **11**, 29–35.
Hutchings, M. T. (1964). In *Solid State Physics*, edited by F. Seitz & D. Turnbull, Vol. 16, pp. 227–273. Academic Press.
Iandelli, A. (1960). *The Physical Chemistry of Metallic Solutions and Intermetallic Compounds*, Vol. 1, pp. 376–376. New York: Chemical Publishing Co.
Iraldi, R., Nguyen, V. N., Rossat-Mignod, J. & Tcheou, F. L. (2008). *Solid State Commun.* **15**, 1543–1546.
Konguetsof, H. & Yakinthos, J. K. (1982). *Phys. Status Solidi A*, **69**, K157–K161.
Liss, K.-D., Hunter, B. A., Hagen, M. E., Noakes, T. J. & Kennedy, S. J. (2006). *Physica B*, **385–386**, 1010–1012.
Litvin, D. B. (1998). *Acta Cryst.* A**54**, 257–261.
Massalski, T. B., Okamoto, H., Subramanian, P. R. & Kacprzak, L. (1990). *Binary Alloy Phase Diagrams*, 2nd ed. Ohio: ASM International.
Mo, Z. J., Shen, J., Yan, L. Q., Tang, C. C., Lin, J., Wu, J. F., Sun, J. R., Wang, L. C., Zheng, X. Q. & Shen, B. G. (2013). *Appl. Phys. Lett.* **103**, 052409.
Nesterov, V. I., Reiman, S. I. & Rozantsev, I. N. (1992). *Sov. Phys. Solid State*, **34**, 671–673.
Nuclear Data Centre Japan (2011). *Online Table of Gamma-ray Energies*. Japan Atomic Energy Agency. https://wwwndc.jaea.go.jp/index.html.
Opechowski, W. & Guccione, R. (1965). *Magnetism*, edited by G. T. Rado and H. Suhl, Vol. 2A, ch. 3. New York: Academic Press.
Perez-Mato, J. M., Gallego, S. V., Tasci, E. S., Elcoro, L., de la Flor, G. & Aroyo, M. I. (2015). *Annu. Rev. Mater. Res.* **45**, 217–248.
Rodríguez-Carvajal, J. (1993). *Physica B*, **192**, 55–69.
Roisnel, T. & Rodríguez-Carvajal, J. (2001). *Mater. Sci. Forum*, **378–381**, 118–123.
Sanchez, J. P., Friedt, J. M., Vasquez, A., L'Héritier, P. & Fruchart, R. (1986). *Solid State Commun.* **57**, 309–313.
Schob, O. & Parthé, E. (1965). *Acta Cryst.* **19**, 214–224.
Shohata, N. (1977). *J. Phys. Soc. Jpn*, **42**, 1873–1880.
Shtender, V., Cedervall, J., Ek, G., Zlotea, C., Andersson, M. S., Manuel, P., Sahlberg, M. & Häussermann, U. (2024). *J. Appl. Cryst.* **57**, 248–257.
Stone, N. J. (2021). *Table of Nuclear Electric Quadrupole Moments*. Technical Report INDC(NDS)-0833. International Nuclear Data Committee, IAEA Vienna.
Susilo, R. A., Cadogan, J. M., Ryan, D. H., Lee-Hone, N. R., Cobas, R. & Muñoz-Pérez, S. (2014). *Hyperfine Interact.* **226**, 257–266.
Susilo, R. A., Pérez, S. M., Cobas, R., Cadogan, J. M. & Avdeev, M. (2012). *J. Phys. Conf. Ser.* **340**, 012071.
Voyer, C. J. & Ryan, D. H. (2006). *Hyperfine Interact.* **170**, 91–104.
Yatsenko, S. P., Semyannikov, A. A., Semenov, B. G. & Chuntonov, K. A. (1979). *J. Less-Common Met.* **64**, 185–199.
Zhang, J. Y., Luo, J., Li, J. B., Liang, J. K., Wang, Y. C., Ji, L. N., Liu, Y. H. & Rao, G. H. (2009). *J. Alloys Compd.* **469**, 15–19.
Zheng, X. Q., Chen, J., Shen, J., Zhang, H., Xu, Z. Y., Gao, W. W., Wu, J. F., Hu, F. X., Sun, J. R. & Shen, B. G. (2012). *J. Appl. Phys.* **111**, 07A917.